Modified nanoplasma model for laser-cluster interaction

S. Micheau, H. Jouin, and B. Pons
CELIA, UMR 5107 Université Bordeaux I, CNRS, CEA, 33405 Talence, France
(Received 4 February 2008; revised manuscript received 10 April 2008; published 16 May 2008)

We present a modified nanoplasma model to describe the interaction of intense laser pulses with rare-gas clusters of nanometric size. Compared to previous models, the model relies on a better description of the collisional processes and allows one to obtain highly charged ion populations and associated x-ray spectra in accordance with experimental findings. We further study the x-ray emission dependence on pulse duration and cluster size and show that these parameters can be optimized to maximize He α production.

DOI: 10.1103/PhysRevA.77.053201 PACS number(s): 36.40.Gk, 52.50.Jm, 52.25.Jm, 52.20.Fs

I. INTRODUCTION

The irradiation of rare-gas clusters by short and intense laser pulses has received a great deal of attention over the past years since experimental findings revealed the peculiar behavior of these targets in the context of laser-matter interaction [1]. Clusters present advantages of both gaseous media and solid targets—i.e., propagation through a large interaction volume and high-energy absorption rates [2], respectively. Experiments have shown that the laser-cluster interaction yields strong (multi-keV) x rays [3], high-order harmonics [4], and very energetic particles [5]. Among these emission processes, we specifically focus on x-ray production. Since targets can be continuously renewed (for example, from the condensation of a high-pressure gas jet expanding through a nozzle [6]) and since no debris is generated [7], the laser-cluster interaction can indeed be thought as an appealing alternative for high-repetition-rate and compact x-ray sources. We further focus on the influence of the laser pulse duration and the cluster size since experiments have shown that the x-ray yield can be enhanced by varying these parameters [8,9].

Several models, based on a fluid description [10], particle-in-cell approach [11,12], or molecular dynamics methods [13–16], have been so far proposed to understand the mechanisms that tailor the laser-cluster interaction, but only a few of them provide detailed information on x-ray emission. Quantitative predictions for x-ray production have been recently obtained using classical transport simulations [17]. The authors identified elastic backscattering of electrons in phase with the oscillating laser field as an efficient heating mechanism, which induces inner-shell processes, resulting in x-ray emission (>3 keV) from highly charged argon ions. Sherrill *et al.* [18] used a coupled electron kinetic and collisional-radiative model to obtain a high-resolution x-ray spectrum. Their simulations describe the dynamics of a nonsteady state Ar^{8+} plasma after the end of the laser pulse. A near-solid density confined during 5.7 ps is found to be necessary to reproduce the experimental spectrum associated with high ionization states.

In this study, we employ the nanoplasma model of Ditmire *et al.* [10] to predict the x-ray production and optimize the emission as a function of laser pulse duration and cluster size. This model is particularly suitable for a description of large clusters (with $N \sim 10^6$, N being the number of atoms in the cluster), which have been shown to favor x-ray emission [9]. The nanoplasma model, which treats the cluster as a dielectric sphere irradiated by the quasistatic laser field, provides a time-dependent picture of the dynamics that other simulations basically corroborate. Moreover, it is convenient for repetitive use because of its simplicity which relies on three main assumptions: (i) the laser field is described within the dipolar approximation, (ii) the electronic and ionic densities are supposed to be uniformly distributed within the cluster throughout the interaction, and (iii) the electrons are assumed to be instantaneously thermalized so that their energy distribution is Maxwellian. Assumption (i) is valid as long as $\lambda \gg R_0$, where λ and R_0 are the laser wavelength and the initial cluster radius, respectively, and the highly collisional nature of the near-solid density nanoplasma dynamics supports assumptions (ii) and (iii). From a practical point of view, the nanoplasma model reduces to a set of differential coupled equations [19] describing the time evolution of the electronic density n_e inside the cluster, which vary due to ionization processes and free streaming, of the populations of the different charge states that evolve through field and collisional ionization, of the net cluster charge, which increases due to free streaming, of the cluster radius, subject to Coulombian and hydrodynamic pressures, and of the electronic temperature T_e, which results from balancing between energy gains and losses within the cluster volume. In a previous contribution [20], we have, however, shown that the original nanoplasma model cannot reproduce the observed high ionization states and associated x-ray spectra. We have traced back the roots of this failure to an incomplete description of the collisional processes. In Sec. II, we detail the ameliorations that have been implemented to improve the description of the nanoplasma dynamics and accordingly provide consistent pictures of the x-ray emission and related spectra. Comparisons of simulations with experimental results as well as optimization of the x-ray yield are presented in Sec. III, and conclusions are drawn in Sec. IV.

II. IMPROVEMENTS

A. Electron-ion collision frequency

First, the electron-ion collision frequency is no longer described in terms of the standard Coulomb formulas of Silin [21], which are inaccurate at high densities. We rather draw

TABLE I. Values of the coefficients C_i used in expressions (3), (5), and (6). Note that the parameters C_5, C_6, and C_7 are valid for an ionic density expressed in cm^{-3}.

C_1	C_2	C_3	C_4	C_5	C_6	C_7
1.042	−0.233	0.139	1.089	2.21×10^{21}	2.78×10^{20}	1.28×10^{22}

from recent works on the heating rate $\partial U/\partial t$ in laser-induced plasmas and relate this one to the frequency ν_{ei}, averaged over one laser cycle [22]:

$$\frac{\partial U}{\partial t} = \frac{4}{3}\nu_{ei}U_P, \tag{1}$$

where $U_P = e^2E^2(t)/4m_e\omega^2$ is the ponderomotive energy and $E(t)$ and ω are the electric field inside the cluster and the laser frequency, respectively. In practice, we use the heating rate of David *et al.* [23], derived from molecular dynamics calculations, in the high-temperature region $\hbar\omega < k_BT_e$, and employ the expression of Polishchuk and Meyer-Ter-Vehn [24] whenever $\hbar\omega > k_BT_e$. Both expressions suitably coalesce in the $\hbar\omega \sim k_BT_e$ transition regime. Moreover, we follow Megi *et al.* [19] who prescribe to introduce an additional damping term, corresponding to electron-surface collisions, to avoid unphysical enhancement of the internal field around the plasmon resonance condition, which occurs when $n_e = 3n_c$, where n_c is the critical density. The electron-ion collision frequency finally reads

$$\nu_{ei} = \frac{8e^4\langle Z\rangle^2}{m_e^2(4\pi\varepsilon_0)^2}\frac{\alpha(n_i)}{v_e^3}\ln\Lambda_1 + \frac{v_e}{R}, \tag{2}$$

where $v_e = (v_{th}^2 + v_{osc}^2)^{1/2}$ is the electronic velocity, v_{th} and v_{osc} are the thermal and cycle-averaged oscillation velocities, respectively, $\langle Z\rangle$ is the mean charge state, and R is the cluster radius. The expression of $\ln\Lambda_1$ varies according to the plasma conditions. We have

$$\ln\Lambda_1 = \ln\left[C_1\xi + C_2\xi^2 + C_3\xi^3 + \exp\left(\frac{1}{3}\sqrt{\pi/2}\right)\right] \times \ln\left[\exp(1) + \frac{k_BT_e}{\hbar\omega}\right] \tag{3}$$

when $\hbar\omega < k_BT_e$, where $\xi = m_ev_{osc}^2/k_BT_e$, and the constants C_i are given in Table I. When $\hbar\omega > k_BT_e$, we get

$$\ln\Lambda_1 = \frac{1}{4}\left[\ln\frac{m_ev_{osc}^2}{\hbar\omega}\right]^2. \tag{4}$$

The function $\alpha(n_i)$ represents the dependence of the heating rate on the ionic density n_i. We use $\alpha(n_i) = n_i$ for $\hbar\omega > k_BT_e$ whereas David *et al.* replace the linear response by a term of the form

$$\alpha(n_i) = C_4n_i\left(1 - \frac{n_i}{C_5}\right) \tag{5}$$

to fit their molecular dynamics data. The coefficients $C_{4,5}$ are given in Table I. This expression is, however, limited to moderate densities since $\alpha(n_i)$ becomes negative when $n_i > 2.21\times10^{21}$ cm^{-3}. As the laser-cluster interaction produces near-solid density plasmas, we extrapolate Eq. (5) to higher densities:

$$\alpha(n_i) = C_6\ln(n_i) - C_7. \tag{6}$$

Expression (5) is used for $n_i < 6\times10^{20}$ cm^{-3}, whereas Eq. (6) is used for higher densities. Both expressions overlap in the intermediate density region.

It has to be noted that expression (2) circumvents the use of the standard Coulomb logarithm, which is negative at the beginning of the interaction—i.e., when the temperature is low and the density is high [10].

B. Unique electron-impact ionization rate

Second, we do not proceed to an artificial discrimination between the so-called thermal and laser collisional ionization rates, as proposed by Ditmire *et al.* We explicitly consider the electron velocity decomposition $\mathbf{v}_e = \mathbf{v}_{th} + \mathbf{v}_{osc}(t)$, where $\mathbf{v}_{th}$ and $\mathbf{v}_{osc}(t) = e\mathbf{E}(t)\cos(\omega t)/m_e\omega$ are the thermal and instantaneous oscillation components, to calculate a unique, and univocally defined, collisional rate as follows: For a given electron temperature T_e, we define the normal distributions associated with the three Cartesian components v_{th_i} $(i = x,y,z)$ of the thermal velocity in terms of discretized distributions of $\mathcal{N}$ independent particles with [25]

$$(v_{th_i})_n = v_{th}(-2\ln U_n)^{1/2}\cos(2\pi U_{n+1}),$$

$$(v_{th_i})_{n+1} = v_{th}(-2\ln U_n)^{1/2}\sin(2\pi U_{n+1}), \tag{7}$$

where $n \in [1,\mathcal{N}-1]$ and U_n are random numbers distributed within $[0,1]$. The total velocity of the nth particle then reads, in the case of a laser field linearly polarized along the $\hat{\mathbf{z}}$ axis,

$$(v_e)_n = \{(v_{e_x})_n^2 + (v_{e_y})_n^2 + [(v_{e_z})_n + v_{osc}(t)]^2\}^{1/2}, \tag{8}$$

where the ωt phase of $\mathbf{v}_{osc}(t)$ is randomly chosen in $[0,2\pi]$ according to the quasistatic hypothesis underlying cycle-averaged rates. The unique collisional rate is then defined as

$$W_{tot} = n_e\langle\sigma(v_e)v_e\rangle_{v_e} = \frac{n_e}{\mathcal{N}}\sum_{n=1}^{\mathcal{N}}\sigma((v_e)_n)(v_e)_n, \tag{9}$$

where $\langle\cdots\rangle_v$ stands for average over the Maxwellian electron distribution and $\sigma(v)$ corresponds to the ionization cross section for an impinging electron with velocity $\mathbf{v}$. In practice, we take $\mathcal{N} = 10\,000$ to accurately fulfill the uniformity of the statistical distributions with respect to all random numbers.

C. Excitation and high-order ionization processes

Third, we include indirect ionization processes. In the original model, high ionic charge states are reached through

successive ionization between ground states, $X^{q+}+e^- \rightarrow X^{(q+1)+}+2e^-$. No allowance is made for indirect pathways involving excited states such as $X^{q+}+e^- \rightarrow X^{q+*}+e^- \rightarrow \cdots \rightarrow X^{(q+1)+}+2e^-$. This is the main reason for the failure of the nanoplasma description to yield high enough charge states insomuch as excitation and ionization collisional rates are of the same order of magnitude. Therefore, we include the high-order ionization processes, but only transitions involving valence electrons are first considered. Thus, neither multiple ionization nor inner-shell processes are taken into account in the ionization dynamics. The former ones are negligible with respect to single ionization, and the latter ones can reasonably be ignored in a first step since the gradually increasing the nanoplasma temperature supports the successive stripping of ions as the main mechanism responsible for the formation of high charged states.

The calculation of both excitation and ionization rates requires the corresponding total cross sections. We work in the single-active electron (SAE) approximation where the interaction of the active (valence) electron with the frozen ion core is described within a model potential approach [26]. The model potential parameters are varied until the eigenvalues of the effective Hamiltonian coincide with the (close-coupling R-matrix) reference data of Seaton [27] and Berrington *et al.* [28], tabulated for the Opacity Project [29], within less than 1%. To further gauge the adequacy of the model potential description, in terms of the accuracy of the approximate wave functions, we have computed the generalized oscillator strengths [30] associated with the optically allowed excitation transitions. Comparison with the reference data [29] is again very satisfactory, as deviations do not exceed a few percent. The empirical formula of Lotz [31] is used for ionization while the excitation cross sections have been computed in the frameworks of distorted-wave Born (DWBA) and plane-wave-Born (PWBA) approximations. The corresponding rates are then calculated following the procedure described in the previous subsection [Eq. (9)].

In nanoplasma simulations, the excitation rates $W_q^{nlm\rightarrow n'l'm'}$ are involved in the temporal dependence of the population $N_{q,nlm}$ of the excited (n,l,m) state of X^{q+} according to

$$\frac{\partial N_{q,nlm}(t)}{\partial t} = \sum_{n'l'm',n'<n} W_q^{n'l'm'\rightarrow nlm} N_{q,n'l'm'}(t) - \sum_{n'l'm',n'>n} W_q^{nlm\rightarrow n'l'm'} N_{q,nlm}(t) - W_q^{nlm\rightarrow\epsilon} N_{q,nlm}(t), \tag{10}$$

where $W_q^{n'l'm'\rightarrow nlm} N_{q,n'l'm'}$ accounts for excitation from lower $(n'<n)$ states and $-W_q^{nlm\rightarrow n'l'm'} N_{q,nlm}$ and $-W_q^{nlm\rightarrow\epsilon} N_{q,nlm}$ describe population losses because of excitation to higher $(n'>n)$ states and ionization, respectively. It is obvious that inclusion of a huge number of (n,l,m)-resolved excited states is, from the computational point of view, prohibitive as it would correspond to a huge set of coupled differential equations. A practical solution, which is commonly used in collisional-radiative modeling of plasmas [32], consists in assuming that the relative populations of states of a given level are close to statistical. We can accordingly carry out a (n,l)-bundling procedure that aggregates the (n,l,m) states into a (nl)-bundled level, whose energy coincides with that of the underlying (n,l,m) states as we do not account for fine structure. (nl)-bundled rates are thus simply defined by

$$W_q^{nl\rightarrow(n'l',\epsilon)} = \frac{1}{2l+1} \sum_{m,m'} W_q^{nlm\rightarrow(n'l'm',\epsilon)}. \tag{11}$$

We can further reduce the number of coupled equations by assuming a statistical distribution within n levels, yielding the n-bundled energies and rates

$$E_n = \frac{1}{n^2} \sum_l (2l+1) E_{nl},$$

$$W_q^{n\rightarrow(n',\epsilon)} = \frac{1}{n^2} \sum_{l,l'} (2l+1) W_q^{nl\rightarrow(n'l',\epsilon)}, \tag{12}$$

where E_{nl} corresponds to the electronic energy of the (n,l,m) states. In practice, we always first proceed to n bundling; more excited n levels are introduced until the convergence of the main populations is reached. Segregation of n-bundled levels into (n,l)- or (n,l,m)-resolved states can later be operated. The excitation processes consistently lead to a decrease of free electron temperature; within a n-bundled approach, the $\partial k_B T_e/\partial t$ associated term reads

$$\sum_q \sum_{n,n'>n} (E_{n'} - E_n) W_q^{n\rightarrow n'} N_{q,n}. \tag{13}$$

Finally, it is worth noting that the dynamics of inner-shell electrons can be similarly described. We shall detail in the next section how we include the dynamics of the $1s$ electrons that monitor the K α emission.

III. RESULTS

A. Ionization dynamics

Including these improvements, we have performed nanoplasma simulations for an argon cluster irradiated by a Ti:sapphire laser pulse. The initial radius of the cluster is $R_0=350$ Å ($N=4.74\times10^6$ atoms), the laser energy is 3 mJ, and the pulse duration [full width at half maximum (FWHM)] is 500 fs, corresponding to a peak intensity of $I_0=1.6\times10^{16}$ W/cm^2. We present in Fig. 1(a) the temporal evolution of the populations N_q of the charge states Ar^{q+} (including both ground and excited states), normalized to the initial number N of atoms. $t=0$ corresponds to the time where the Gaussian laser field reaches its maximum value. To obtain a converged description of ionization, it has been necessary to include the $n=4$ bundled level for $q=1$, the $n=4,5$ ones for $q=2$, $n=4-6$ for $3\leq q\leq 7$, $n=3-6$ for $8\leq q\leq 11$, and 6 excited n levels for $q\geq 12$. This corresponds to 1840 (n,l,m)-resolved states. In previous calculations performed under similar laser and cluster conditions, we have shown that the original nanoplasma model leads to Ar^{q+}-ion

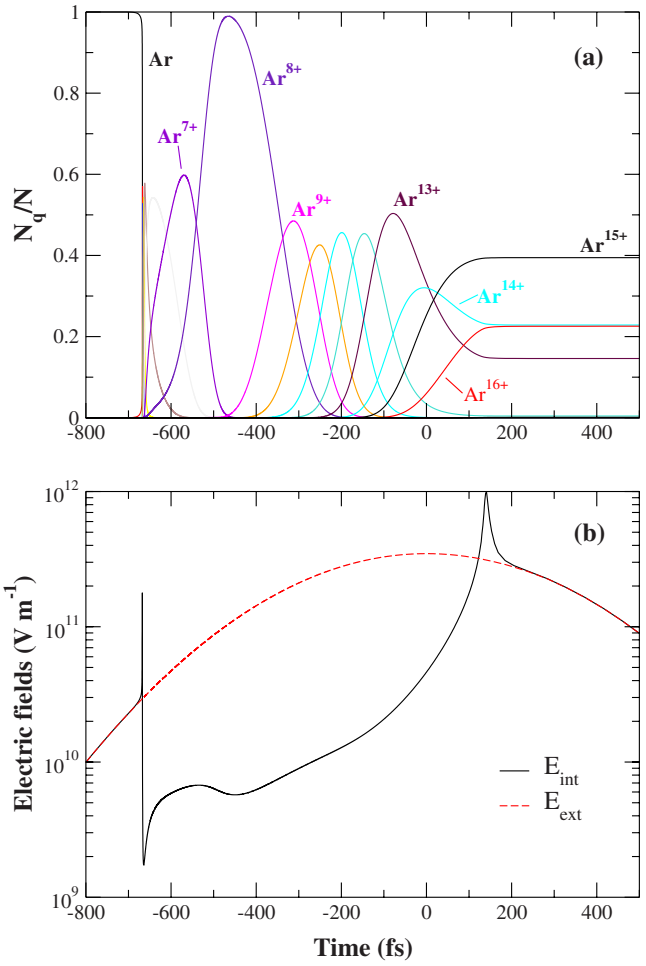

FIG. 1. (Color online) Temporal evolution of (a) the populations of Ar^{q+} normalized to the initial number of atoms and (b) internal and laser electric field amplitudes, obtained by means of the modified nanoplasma model for an argon cluster ($R_0=350$ Å) irradiated by a Ti:sapphire laser ($\tau=500$ fs, $I_0=1.6\times10^{16}$ W/cm^2, $E=3$ mJ).

charge states with $q\leq13$, whereas experimental results indicate x-ray emission from highly charged ions with $q\leq16$ [20]. The striking feature of Fig. 1 is the production of highly populated Ar^{q+} charge states up to $q=16$. We can further underline the impact of the model's improvements previously detailed by evaluating the mean charge state $\langle q\rangle$ at the end of the laser-cluster interaction. In Fig. 1, $\langle q\rangle=14.7$ whereas the original model leads to $\langle q\rangle=10.9$ only.

To depict the dynamics of the laser-cluster interaction, we show in Fig. 1(b) the temporal evolution of the internal and laser electric fields. At $t=-800$ fs, the inner field $E_{int}(t)$ (which is almost equal to the laser field since the electronic density n_e is very low) becomes large enough to induce tunneling ionization of the Ar atoms. The electronic density accordingly increases and rapidly reaches the particular value $n_e=3n_c=5.2\times10^{21}$ cm^{-3}, where n_c is the critical density and $3n_c$ corresponds to the plasmon resonance where the internal field is strongly enhanced. The first Ar^{q+} charge states are thus almost instantaneously ionized up to $q=4$ until n_e becomes larger than $3n_c$ at $t=-670$ fs. The internal electric field is then strongly shielded with respect to the laser one and becomes too low to further populate higher charge states. Nevertheless, as the electrons mainly gain energy through inverse bremsstrahlung (IB), the electronic temperature T_e roughly follows the evolution of the inner field. The progressive increase of T_e thus induces direct or indirect (i.e., through intermediate excited states) electron-impact ionization that leads to higher ionized states. In the meanwhile, electrons with enough energy can leave the cluster. The Coulombian pressure induced by this loss of plasma neutrality combined with the T_e-mediated hydrodynamic pressure induces the expansion of the nanoplasma. n_e accordingly decreases until it approaches the $n_e=3n_c$ resonance condition at $t=142$ fs. The enhancement of the inner field then leads to a very efficient absorption of the laser energy, resulting in a high-temperature (several keV) electron bath, which produces the highest charge states up to $q=16$. However, the important free streaming that arises from the growing temperature and the associated sudden increase of the Coulombian pressure end at time $t=140$ fs in the final explosion of the cluster.

B. X-ray spectrum

We now turn to the ability of our model to yield the theoretical counterparts to the time-integrated x-ray spectra obtained in laser-cluster experiments (see, e.g., [9,20]). Experiments indicate that energetic x rays (>3 keV) arise from K α transitions. As our calculations explicitly include the $1s\rightarrow2p$ excitation process in Ar^{16+}, little effort is required to evaluate the He α emission. We segregate the $n=2$ bundled level into $2p$ and $2s$ states, and compute the Einstein spontaneous decay rate $A_{16}^{2p\rightarrow1s}$ in the context of the model potential approach. The other K α lines are related to inner-shell $1s$ vacancies and subsequent $2p\rightarrow1s$ radiative deexcitation. To describe them, we introduce in our set of coupled equations an additional excited state for each of the Ar^{q+} ions with $9\leq q\leq15$, representing an excited electron on the $2p$-shell and associated $1s$-shell vacancies. We consider that these levels are populated from the ground states through collisional excitation and decay either radiatively or through Auger relaxation according to

$$\frac{\partial N_{q,2p}(t)}{\partial t}=W_q^{1s\rightarrow2p}N_{q,1s}(t)-A_q^{2p\rightarrow1s}N_{q,2p}(t)-W_q^{Auger,2p}N_{q,2p}(t). \quad (14)$$

$N_{q,1s}$ and $N_{q,2p}$, respectively, stand for the populations of the ground and $1s2p$ excited states of an Ar^{q+} ion, $W_q^{1s\rightarrow2p}$ is the collisional excitation rate, and $A_q^{2p\rightarrow1s}$ and $W_q^{Auger,2p}$ are the Einstein spontaneous and Auger decay rates. Rather than introducing additional model potentials to determine those rates, we have used the recommended data of the International Atomic Energy Agency [33]. By integrating over time the radiative decays, we then evaluate the number of K α photons emitted for each ion:

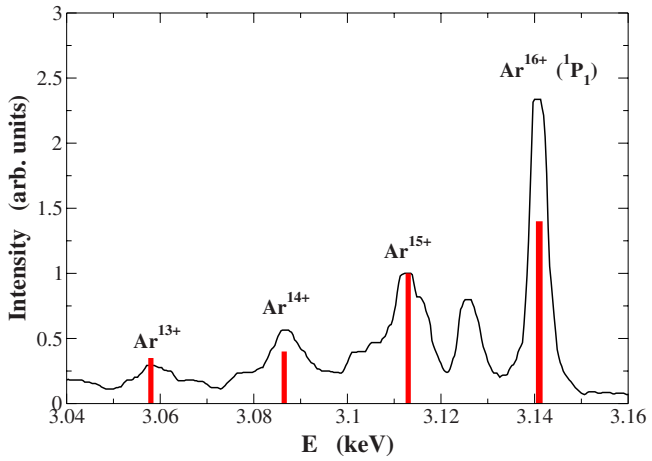

FIG. 2. (Color online) Experimental [20] and theoretical x-ray spectra obtained under the same conditions as Fig. 1.

$$N_{\mathrm{K}\,\alpha}^{(q)} = \int_{-\infty}^{+\infty} dt\, A_q^{2p\to 1s} N_{q,2p}(t). \tag{15}$$

Figure 2 shows the experimental x-ray spectrum obtained with the same parameters as in Fig. 1 and the number of K α photons theoretically obtained for each ion. It has to be noted that the triplet Ar^{16+} excited state is not included in our calculations so that we cannot retrieve the intercombination line at 3.125 keV. The results obtained, normalized to the Ar^{15+} line, indicate that our model correctly reproduces the experimental spectrum, as the K α emission increases with the ion charge. It is interesting to note that, even though there are more Ar^{15+} than Ar^{16+} ions (see Fig. 1), the He α line is brighter than the Li α one. This is due to higher collisional excitation and radiative decay rates.

C. Influence of the laser pulse duration

Dorchies *et al.* have reported measurements of the x-ray signal in the He α line (3.14 keV) as a function of the pulse duration τ for a fixed energy of 3 mJ [20]. Their results are shown in Fig. 3, which also includes the theoretical time-integrated He α signal obtained by means of our model according to Eq. (15). The theoretical results have been averaged over Gaussian cluster size and intensity spatial distributions in order to mimic the experimental uncertainty

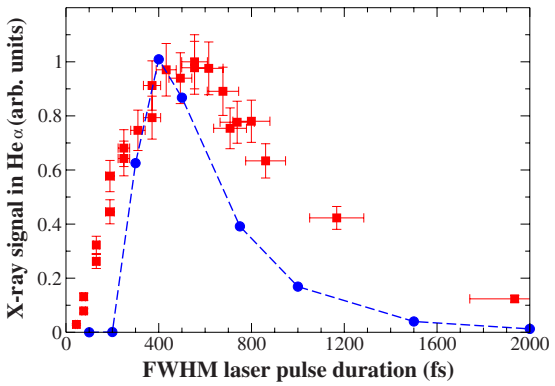

FIG. 3. (Color online) Intensity of He α emission as a function of FWHM pulse duration for an argon cluster with mean radius R_0=350 Å. The laser energy is 3 mJ for all pulse durations. Experimental (■) and theoretical (dot-dashed line) results.

$R_0=(350\pm 38)$ Å [20] and to account for the location of the cluster within the focal volume. The modified nanoplasma model reproduces the behavior of the experimental results with the advent of an optimum laser pulse duration for the He α signal. Although the theoretical optimum is slightly shorter than the experimental one, the overall agreement is yet satisfactory, and this justifies our confidence in the reliability or our description of both heating and ionization dynamics.

To understand the occurrence of an optimum pulse duration, we compare in Fig. 4, for R_0=350 Å and a fixed energy of 3 mJ, the temporal evolution of the laser and inner fields for τ=200 and 1000 fs. t=0 has been set by reference to the time where $E_{las}=10^{10}$ V/m for convenience of comparison. The advent of the optimum pulse duration results from the interplay of ionization and (resonant) efficient heating. As the laser energy is fixed, the shorter the pulse duration, the prompter are the increase and decrease of the laser field amplitudes. For a 200-fs pulse [Fig. 4(a)], the quicker rising field leads to faster ionization dynamics. Nevertheless, short pulse durations impede enhanced electron heating since the $n_e=3n_c$ resonant absorption condition occurs as the laser field has decreased to a small value. So short pulse durations allow a sizable production of highly charged ions up to Ar^{16+}, but the low electron temperature (<500 eV) clamps the excitation of these ions and accordingly prevents strong x-ray emission. Reversely, longer pulse durations [Fig. 4(b)] severely slow down ionization and accordingly yield a tiny

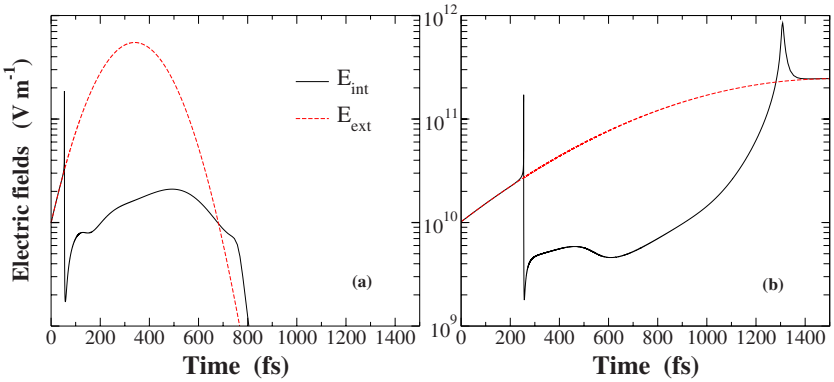

FIG. 4. (Color online) Laser and internal electric field amplitudes in Ti:sapphire laser–Ar-cluster interaction. The mean radius is R_0=350 Å. The laser energy is 3 mJ, and two pulse durations of (a) 200 fs and (b) 1 ps corresponding, respectively, to the maximum pulse intensities $I_0=4\times 10^{16}$ and 8×10^{15} W/cm^2.

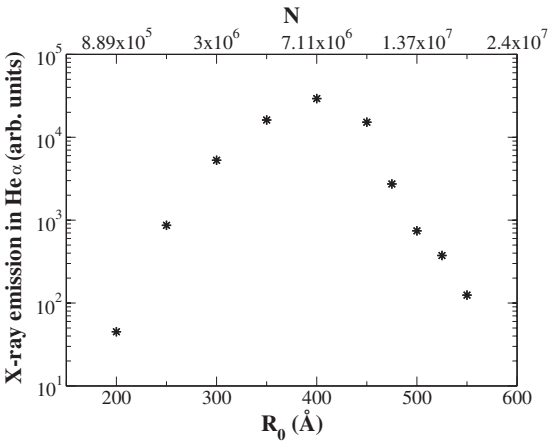

FIG. 5. Intensity of He α emission as a function of initial argon cluster size for fixed laser parameters ($I_0=1.6\times10^{16}$ W/cm^{-2}, $\tau=300$ fs, $E=3$ mJ).

Ar^{16+} population at the moment where efficient electron heating takes place.

D. Influence of cluster size

It is further interesting to investigate the dependence of the x-ray emission on the cluster size. Several experiments have shown that the x-ray yield increases with the number of atoms compounding the clusters [9,20,34]. These experiments have, however, been limited to $R_0\leq350$ Å. Using our modified nanoplasma model, we have performed calculations to study the evolution of the number of He α photons emitted as a function of the cluster radius. Our model allows us to extend the cluster size range to determine optimal conditions for x-ray emission and guide future experiments. The results obtained for fixed laser parameters ($I_0=1.6\times10^{16}$ W/cm^{-2}, $\tau=300$ fs, $E=3$ mJ) are shown in Fig. 5. In agreement with the experimental results, the x-ray yield increases with the cluster size as long as $R_0\leq400$ Å. Further increase of the initial radius, however, leads to lower emission, indicating an optimum cluster size. To understand the emergence of this optimum, one has to consider that the expansion of the cluster is driven by hydrodynamic and Coulombian pressures. As these pressures, respectively, vary as R^{-3} and R^{-4}, the smaller the cluster, the faster it expands. For a given pulse duration, the $n_e=3n_c$ resonance condition and, hence, the final explosion are thus more rapidly reached as the cluster size decreases. On the one hand, the end of the interaction occurs too early for a small cluster so that the ionization dynamics is shortened and the highly charged ion populations are accordingly low. On the other hand, the expansion time of larger clusters is severely enlarged so that the resonance condition is reached when the electric field is weak and the corresponding low electron heating impedes strong x-ray emission.

IV. CONCLUDING REMARKS

In conclusion, we have improved the nanoplasma model with a more complete description of the collisional processes. Particular allowance has been made for high-order ionization processes involving valence electrons to improve the production of high charge states, and the dynamics of inner-shell electrons has been partially included to reproduce the K α x-ray emission. With this model, we have been able to reproduce the main features of x-ray spectra emitted by Ar clusters. We have also reproduced the experimental He α emission dependence on pulse duration and cluster size and further shown that these parameters can be optimized to maximize the He α production. Nevertheless, it has to be noted that our model yields insignificant K α emission for short pulse durations ($\tau\leq200$ fs; see Fig. 3) and/or weak laser fields ($I_0\sim10^{14}$ W/cm^2). The IB heating is not efficient enough under such irradiation conditions, and additional heating mechanisms such as the Fermi shuttle [17] or locally enhanced electric fields induced by density inhomogeneities [11] may then play a decisive role since the beginning of the interaction. The inclusion of such mechanisms in the nanoplasma description is not easily feasible since they are not compatible with the assumptions of homogeneous velocity and density. From a practical point of view, this inclusion is fortunately unnecessary: in the small τ and/or I_0 regime, reliable simulations have to be performed in terms of sophisticated particle-in-cell, molecular dynamics, or classical transport methods, which intrinsically include both IB and additional heating mechanisms. For longer and intense pulses, our nanoplasma model, which self-consistently couples the nanoplasma dynamics and the collisional-radiative processes, safely applies because of the leading role of the IB mechanism. The validity range of our model encompasses the optimum irradiation and cluster conditions leading to maximum K α emission, and the model can be easily implemented to large rare-gas clusters other than Ar ones because of its enhanced versatility.

[1] A. McPherson, T. S. Luk, B. D. Thompson, K. Boyer, and C. K. Rhodes, Appl. Phys. B: Lasers Opt. **57**, 337 (1993).
[2] T. Ditmire, R. A. Smith, J. W. G. Tisch, and M. H. R. Hutchinson, Phys. Rev. Lett. **78**, 3121 (1997).
[3] A. McPherson, T. S. Luk, B. D. Thompson, A. B. Borisov, O. B. Shiryaev, X. Chen, K. Boyer, and C. K. Rhodes, Phys. Rev. Lett. **72**, 1810 (1994).
[4] T. D. Donnelly, T. Ditmire, K. Neuman, M. D. Perry, and R. W. Falcone, Phys. Rev. Lett. **76**, 2472 (1996).
[5] Y. L. Shao, T. Ditmire, J. W. G. Tisch, E. Springate, J. P. Marangos, and M. H. R. Hutchinson, Phys. Rev. Lett. **77**, 3343 (1996).
[6] O. F. Hagena and W. Obert, J. Chem. Phys. **56**, 1793 (1972).
[7] F. Jin and M. Richardson, Appl. Opt. **34**, 5750 (1995).
[8] J. Zweiback, T. Ditmire, and M. D. Perry, Phys. Rev. A **59**, R3166 (1999).

[9] S. Dobosz, M. Lezius, M. Schmidt, P. Meynadier, M. Perdrix, D. Normand, J. P. Rozet, and D. Vernhet, Phys. Rev. A **56**, R2526 (1997).
[10] T. Ditmire, T. Donnelly, A. M. Rubenchik, R. W. Falcone, and M. D. Perry, Phys. Rev. A **53**, 3379 (1996).
[11] Y. Fukuda, Y. Kishimoto, T. Masaki, and K. Yamakawa, Phys. Rev. A **73**, 031201(R) (2006).
[12] C. Jungreuthmayer, M. Geissler, J. Zanghellini, and T. Brabec, Phys. Rev. Lett. **92**, 133401 (2004).
[13] C. Rose-Petruck, K. J. Schafer, K. R. Wilson, and C. P. J. Barty, Phys. Rev. A **55**, 1182 (1997).
[14] K. Ishikawa and T. Blenski, Phys. Rev. A **62**, 063204 (2000).
[15] I. Last and J. Jortner, Phys. Rev. A **62**, 013201 (2000).
[16] C. Siedschlag and J. M. Rost, Phys. Rev. Lett. **89**, 173401 (2002).
[17] C. Deiss, N. Rohringer, J. Burgdörfer, E. Lamour, C. Prigent, J.-P. Rozet, and D. Vernhet, Phys. Rev. Lett. **96**, 013203 (2006).
[18] M. E. Sherrill, J. Abdallah, Jr., G. Csanak, E. S. Dodd, Y. Fukuda, Y. Akahane, M. Aoyama, N. Inoue, H. Ueda, K. Yamakawa, A. Ya. Faenov, A. I. Magunov, T. A. Pikuz, and I. Yu. Skobelev, Phys. Rev. E **73**, 066404 (2006).
[19] F. Megi, M. Belkacem, M. A. Bouchene, E. Suraud, and G. Zwicknagel, J. Phys. B **36**, 273 (2003).
[20] F. Dorchies, T. Caillaud, F. Blasco, C. Bonté, H. Jouin, S. Micheau, B. Pons, and J. Stevefelt, Phys. Rev. E **71**, 066410 (2005).
[21] V. P. Silin, Sov. Phys. JETP **20**, 1510 (1965).
[22] P. Mulser, F. Cornolti, E. Bésuelle, and R. Schneider, Phys. Rev. E **63**, 016406 (2000).
[23] N. David, D. J. Spence, and S. M. Hooker, Phys. Rev. E **70**, 056411 (2004).
[24] A. Y. Polishchuk and J. Meyer-Ter-Vehn, Phys. Rev. E **49**, 663 (1994).
[25] *Handbook of Mathematical Functions*, edited by M. Abramovitz and I. Stegun (Dover, New York, 1972).
[26] M. Klapisch, Comput. Phys. Commun. **2**, 239 (1971).
[27] M. J. Seaton, J. Phys. B **20**, 6363 (1987).
[28] K. A. Berrington, P. G. Burke, K. Butler, M. J. Seaton, P. J. Storey, K. T. Taylor, and Y. Yan, J. Phys. B **20**, 6379 (1987).
[29] C. Mendoza, C. Zeippen, and A. Pradhan, The Opacity Project, http://cdsweb.u-strasbg.fr/topbase/topbase.html
[30] H. A. Bethe and E. E. Salpeter, *Quantum Mechanics of One- and Two-Electron Atoms* (Plenum, New York, 1977).
[31] W. Lotz, Z. Phys. **216**, 241 (1968).
[32] H. P. Summers, W. J. Dickson, M. G. O'Mullane, N. R. Badnell, A. D. Whiteford, D. H. Brooks, J. Lang, S. D. Loch, and D. C. Griffin, Plasma Phys. Controlled Fusion **48**, 263 (2006).
[33] http://www-amdis.iaea.org
[34] V. Kumarappan, M. Krishnamurthy, D. Mathur, and L. C. Tribedi, Phys. Rev. A **63**, 023203 (2001).